

Data-Driven Discovery of Transition Metal Dichalcogenide-Based Z-Scheme Photocatalytic Heterostructures

Xiaoqing Liu, Yi-Ming Zhao, Xiuying Zhang, Lin Wang, Jiadong Shen, Miao Zhou,* and Lei Shen*



Cite This: ACS Catal. 2023, 13, 9936–9945



Read Online

ACCESS |
Metrics & More
Article Recommendations
Supporting Information

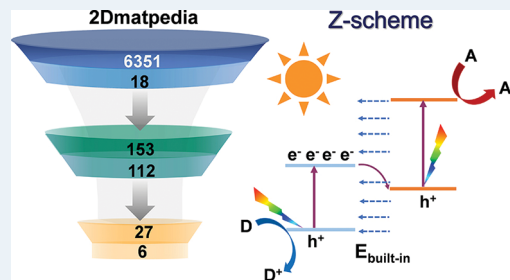
ABSTRACT: The Z-scheme heterostructure is a highly promising photocatalyst for its unique electronic structure. However, a thorough examination of the heterostructure design space through experimental or computational means is prohibitively expensive. Here, we propose a highly efficient data-driven approach for fast discovering van der Waals (vdW) Z-scheme heterostructures, bypassing the need for costly calculations and experimentation. By conducting high-throughput calculations with the Heyd–Scuseria–Ernzerhof hybrid density functional (HSE06), we first generate a variety of data of electronic structures for 18 experimentally synthesized 2D transition metal dichalcogenides (TMDs) and 20 of 153 heterostructures (constructed with the 18 TMDs). Using these data, we develop an innovative and robust descriptor: Allen “material” electronegativity. Leveraging this descriptor, we identify 27 2D vdW Z-scheme heterostructures from the pool of 153 heterostructures without expensive HSE calculations. We finally refine our findings by selecting six Z-scheme heterostructures with minimal lattice mismatch, further validating them using high-fidelity *ab initio* calculations and studying their optical absorption. Our research not only paves the way for discovering high-performance Z-scheme photocatalysts using data-driven methods but also contributes a universal charge transfer mechanism for vdW device applications.

KEYWORDS: *transition metal dichalcogenides, Z-scheme heterostructure, photocatalyst, material descriptor, high-throughput calculations*

INTRODUCTION

Photocatalytic technology has emerged as a promising sustainable strategy for addressing the pressing concerns of environmental pollution and global fossil fuel depletion.^{1,2} Z-Scheme heterostructures have attracted considerable attention in the field of photocatalytic technology due to their broad solar absorption spectrum and preserve photogenerated reaction carriers with strong redox capability.^{3–9} The mechanism and key criteria of Z-scheme heterostructures share similarities with conventional type-II heterostructures in terms of band alignment but exhibit distinctly different photogenerated carrier transfer pathways (see in Scheme 1). To enable such a charge transfer mechanism, the Z-scheme heterostructure must have a small band alignment (δ) and a large directional built-in electric field ($E_{\text{built-in}}$). Consequently, photogenerated electrons and holes with a large redox potential are well-preserved and spatially separated within the Z-scheme heterostructure (Scheme 1).^{10–12} Combining two narrow bandgap semiconductors into a Z-scheme heterostructure may resolve the dilemma of single-material or type-II photocatalysts, where strong redox capability and a broad light absorption range cannot be achieved simultaneously.^{13–16} Therefore, the discovery and design of Z-scheme heterostructures for photocatalysis is of critical importance.

Instead of relying on the resource-intensive trial-and-error approach of stacking various 2D materials to identify van der Waals (vdW) Z-scheme heterostructures, the data-driven



approach can significantly streamline the design process. The availability of well-developed 2D materials databases, such as 2DMatPedia, C2DB, and JARVIS, allows researchers to access various properties of over 6000 2D materials, such as the exfoliation energy, decomposition energy, band structure, and work function.^{17–24} By leveraging these available properties, one may derive effective and practical descriptors for evaluating interfacial electric fields and band alignments of vdW 2D heterostructures, enabling the quick identification of Z-scheme photocatalysts before contact (as illustrated in Scheme 1), without resorting to computationally expensive high-fidelity density functional theory (DFT) calculations, such as GW and Heyd–Scuseria–Ernzerhof hybrid functionals (HSE). The primary challenge lies in predicting the built-in electric field of a vdW 2D heterostructure before contact, including the magnitude and direction of charge transfer. Recent efforts have sought descriptors for charge transfer in vdW 2D heterostructures, including differences in work functions (ΔW), covalent radii (ΔR), and Pauling atomic electronegativities ($\Delta \chi$) between two 2D materials.^{25–28}

Received: May 22, 2023

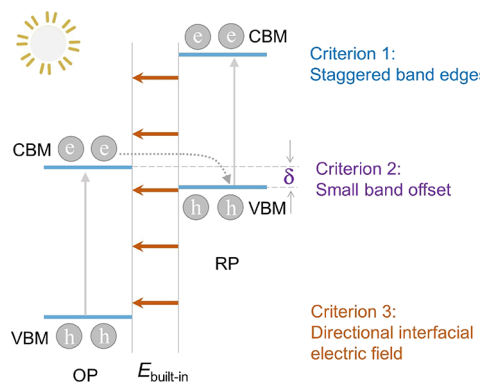
Revised: July 4, 2023

Published: July 14, 2023


ACS Publications

© 2023 American Chemical Society

Scheme 1. Schematic Z-Scheme Heterostructure and Its Three Key Criteria^a



^aOP and RP represent the oxidation and reduction photocatalyst, respectively. $E_{\text{built-in}}$ denotes the interfacial built-in electric field, which is induced by the intrinsic charge transfer between the two photocatalysts after contact. The high separation efficiency of electron–hole pairs in the Z-scheme heterostructure is attributed to its small band offset and large directional interfacial electric field. A critical question raised is whether it is possible to obtain these parameters, especially criterion 3 (the interfacial electric field), before forming a heterostructure, thereby avoiding the need for costly heterostructure-based calculations.

However, these descriptors are either inapplicable or imprecise for distinguishing Z-scheme heterostructures from other categories, particularly from their type-II heterostructure parents as they share the same ΔW , ΔR , and $\Delta \chi$.

In this work, we first calculate the HSE electronic structure of 18 experimentally synthesized H-phase transition metal dichalcogenides (TMD), namely, HfTe₂, MoS₂, TiSe₂, WSe₂, ZrSe₂, CrSe₂, HfSe₂, TiTe₂, WTe₂, ZrS₂, CrTe₂, HfS₂, TiS₂, WS₂, CrS₂, MoSe₂, MoTe₂, and ZrTe₂ (see details in Table 1).^{29,30} Using their HSE electronic structures and Anderson's

rule, we screen 112 of the 153 heterostructures (formed by the 18 TMDs) with type-II band alignment. Next, we select 20 of the 112 type-II heterostructures and systematically calculate their HSE electronic structures, amount of charge transfer, and built-in interfacial electric field (see details in Table 2). Leveraging the high-fidelity data from the 18 TMDs and 20 vdW heterostructures, we develop a novel descriptor known as Allen “material” electronegativity ($\Delta \chi_m$). It is important to note that this differs from the traditional concept of Pauling electronegativity, which applies to atoms. The material electronegativity enables us to further identify a total of 27 Z-scheme candidates from 112 type-II heterostructures bypassing the need for expensive HSE calculations on large supercells of heterostructures. Among them, three have been previously reported in the literature, while the remaining 24 have never been reported hitherto. We finally refine the 27 candidates by selecting six Z-scheme heterostructures (TiS₂/CrSe₂, TiS₂/MoS₂, TiS₂/MoSe₂, TiSe₂/MoSe₂, TiS₂/WS₂, and TiSe₂/WSe₂) with minimal lattice mismatch and verify them by DFT calculations. Our optical calculations show that TiS₂/CrSe₂ has near-infrared light absorption and large reaction driving force, showing enormous potential for photocatalytic applications. The data-driven discovery of effective descriptors not only provides new high-potential Z-scheme heterostructure candidates but also offers a simple yet effective means of accelerating future development of solar-to-hydrogen, CO₂, and other essential photocatalysis reactions.

COMPUTATIONAL DETAILS

DFT calculations were executed using the Vienna *ab initio* simulation package (VASP).³¹ The core-electron interactions were described by the frozen-core projector augmented wave (PAW) method.³² The electronic exchange-correlation energy was treated using the generalized gradient approximation in the form of Perdew–Burke–Ernzerhof (GGA-PBE) formalism.³³ The Heyd–Scuseria–Ernzerhof hybrid density functional

Table 1. The Calculated Lattice (Å), Band Gap (eV), Gap Type, Band Alignment of the VBM and CBM with Respect to the Vacuum Level, and Magnetism of 18 Experimentally Synthesized 2H-Phase TMD Semiconductors Used in This Work as Building Blocks for Constructing vdW Heterostructures^a

2H-TMD	lattice	HSE band gap	gap type	VBM	CBM	magnetism	experiment
HfTe ₂	$a = b = 3.91$	1.19	indirect	-6.40	-5.20	NM	ref 29
MoS ₂	$a = b = 3.18$	2.10	direct	-6.70	-4.59	NM	ref 29
TiSe ₂	$a = b = 3.50$	1.60	indirect	-7.10	-5.51	NM	ref 29
WSe ₂	$a = b = 3.32$	1.96	direct	-5.82	-3.86	NM	ref 29
ZrSe ₂	$a = b = 3.70$	1.67	indirect	-7.28	-5.62	NM	ref 29
CrSe ₂	$a = b = 3.21$	1.04	direct	-6.02	-4.98	NM	ref 29
HfSe ₂	$a = b = 3.68$	1.74	indirect	-7.31	-5.57	NM	ref 29
TiTe ₂	$a = b = 3.74$	1.30	indirect	-6.31	-5.01	NM	ref 29
WTe ₂	$a = b = 3.55$	1.41	direct	-5.26	-3.85	NM	ref 29
ZrS ₂	$a = b = 3.57$	1.96	indirect	-7.90	-5.94	NM	ref 29
CrTe ₂	$a = b = 3.47$	0.89	direct	-5.44	-4.55	NM	ref 30
HfS ₂	$a = b = 4.31$	2.05	indirect	-7.94	-5.90	NM	ref 29
TiS ₂	$a = b = 3.35$	1.78	indirect	-7.76	-5.99	NM	ref 29
WS ₂	$a = b = 3.19$	2.28	direct	-6.45	-4.17	NM	ref 29
CrS ₂	$a = b = 3.05$	1.24	direct	-6.64	-5.40	NM	ref 30
MoSe ₂	$a = b = 3.32$	1.83	direct	-6.06	-4.23	NM	ref 29
MoTe ₂	$a = b = 3.55$	1.43	direct	-5.48	-4.05	NM	ref 29
ZrTe ₂	$a = b = 3.92$	1.25	indirect	-6.49	-5.24	NM	ref 29

^aThe HSE hybrid functional is used in this work for getting more accurate electronic structures of these 2D semiconductors. NM means nonmagnetism.

Table 2. Structural Details and HSE Calculation Results of 20 Samples of Heterostructure Supercells, Including the Acceptor and Donor in a Heterostructure, the Size of the Supercell, the Total Number of Atoms in the Supercell, the Lattice Mismatch between Two Materials, the Distance between Two Materials (Δd in Å), and the Binding Energy E_b of Two Materials in meV^a

acceptor–donor	supercell	lattice (Å)	atoms	mismatch	Δd	E_b	E_g (eV)	$\Delta\chi_m$	ΔQ (e)
MoS ₂ /TiSe ₂	$3 \times 3 \times 1/\sqrt{7} \times \sqrt{7} \times 1$	9.48	48	3.19%	3.40	-31.14	1.11	0.061	0.084
MoS ₂ /ZrSe ₂	$2 \times 2 \times 1/\sqrt{3} \times \sqrt{3} \times 1$	6.41	21	-0.89%	3.43	-32.00	1.09	0.052	0.033
MoS ₂ /HfSe ₂	$2 \times 2 \times 1/\sqrt{3} \times \sqrt{3} \times 1$	6.39	21	0.04%	3.44	-31.44	1.14	0.059	0.049
TiS ₂ /MoS ₂	$1 \times 1 \times 1/1 \times 1 \times 1$	3.27	6	-4.97%	3.60	-27.23	0.72	0.079	0.001
MoS ₂ /WSe ₂	$1 \times 1 \times 1/1 \times 1 \times 1$	3.27	6	-4.18%	3.79	-25.74	0.76	0.124	0.004
MoS ₂ /WTe ₂	$2 \times 2 \times 1/\sqrt{3} \times \sqrt{3} \times 1$	6.32	21	3.12%	3.71	-30.98	1.01	0.314	0.101
WS ₂ /MoS ₂	$1 \times 1 \times 1/1 \times 1 \times 1$	3.20	6	-0.06%	3.74	-25.18	0.99	0.121	0.013
MoS ₂ /MoSe ₂	$1 \times 1 \times 1/1 \times 1 \times 1$	3.26	6	-4.20%	3.80	-25.67	1.22	0.308	0.102
MoS ₂ /MoTe ₂	$2 \times 2 \times 1/\sqrt{3} \times \sqrt{3} \times 1$	6.32	21	3.13%	3.69	-30.92	1.13	0.123	0.020
CrS ₂ /TiSe ₂	$2 \times 2 \times 1/\sqrt{3} \times \sqrt{3} \times 1$	6.11	21	-0.68%	3.51	-30.32	0.69	0.016	0.115
TiS ₂ /CrS ₂	$\sqrt{7} \times \sqrt{7} \times 1/3 \times 3 \times 1$	9.06	48	-3.37%	3.27	-30.04	0.76	0.060	0.003
TiSe ₂ /MoSe ₂	$1 \times 1 \times 1/1 \times 1 \times 1$	3.42	6	5.26%	3.80	-28.30	0.53	0.063	0.028
TiSe ₂ /WSe ₂	$1 \times 1 \times 1/1 \times 1 \times 1$	3.41	6	5.28%	3.80	-28.15	0.62	0.093	0.020
ZrS ₂ /WS ₂	$\sqrt{3} \times \sqrt{3} \times 1/2 \times 2 \times 1$	6.33	21	2.86%	3.39	-31.00	0.81	0.088	0.003
HfS ₂ /MoS ₂	$\sqrt{3} \times \sqrt{3} \times 1/2 \times 2 \times 1$	6.29	21	4.01%	3.40	-30.56	0.90	0.026	0.006
HfS ₂ /CrS ₂	$\sqrt{3} \times \sqrt{3} \times 1/2 \times 2 \times 1$	6.13	21	0.18%	3.41	-29.96	0.79	0.031	0.015
ZrS ₂ /CrS ₂	$2 \times 2 \times 1/\sqrt{3} \times \sqrt{3} \times 1$	6.16	21	1.45%	3.37	-30.47	1.79	-0.001	0.001
TiS ₂ /CrSe ₂	$1 \times 1 \times 1/1 \times 1 \times 1$	3.23	6	-3.83%	3.68	-28.21	0.76	0.134	0.046
TiS ₂ /WS ₂	$1 \times 1 \times 1/1 \times 1 \times 1$	3.36	6	0.56%	3.63	-27.12	0.23	0.079	0.010
TiS ₂ /MoSe ₂	$1 \times 1 \times 1/1 \times 1 \times 1$	3.36	6	4.68%	3.70	-28.17	0.32	0.200	0.034

^aFurthermore, the calculated HSE06 band gap, the Allen material electronegativity difference $\Delta\chi_m$ between two materials, and the calculated amount of Bader charge transfer ΔQ between the donor and acceptor are also given in the table below.

(HSE06) was used to obtain the accurate band gap and band edges.^{34,35} The optPBE exchange-correlation energy was employed, incorporating vdW interaction corrections.³⁶ The plane-wave cutoff energy was set to 500 eV, and the Brillouin zone was integrated using Gamma-centered grids with consistent spacing density for all cell sizes (KSPACING = 0.25 Å⁻¹ for geometric optimization). A vacuum layer of 15 Å in the Z-direction was introduced to prevent spurious interactions between adjacent slabs. For geometry optimization, convergence criteria of energy and forces acting on each atom were set at 10⁻⁴ eV and 0.01 eV Å⁻¹. Atomic positions and charge density illustrations were obtained using VESTA.³⁷ Further analysis was conducted using the postprocessing program VASPKIT.³⁸ Partial atomic charges were obtained using Bader charge analysis as implemented by Henkelman and coworkers.^{39–41}

RESULTS AND DISCUSSION

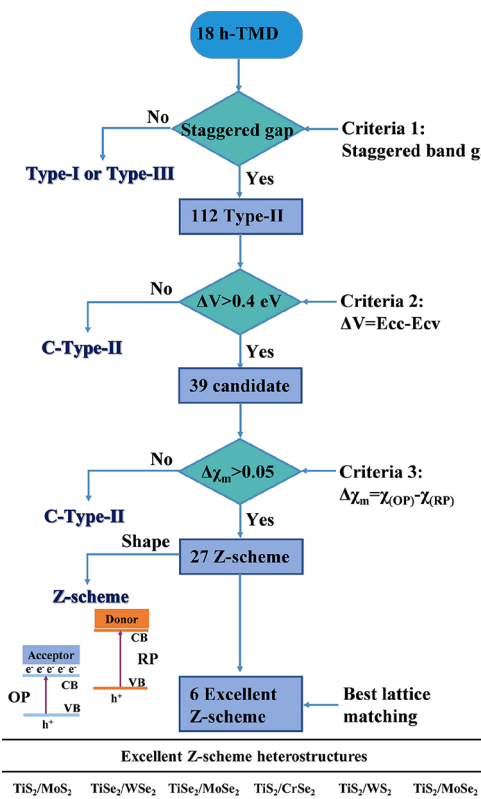
Based on the Z-scheme photocatalytic mechanism (Scheme 1), three key characteristics are deemed necessary. Criterion 1 is the prerequisite that a staggered band alignment is the main feature for a type-II heterostructure. Criterion 2 involves a small band offset for a low energy barrier. The directional interfacial electronic field is the most crucial criterion 3 for identifying the Z-scheme heterostructure. A larger charge transfer from RP to OP results in a stronger built-in electric field, which is critical for facilitating the combination of “useless” photogenerated electrons at OP and holes at RP.⁴² This study aims to develop effective descriptors for accelerating the screening process for identifying TMD-based Z-scheme heterostructures.

Based on the three criteria discussed in Scheme 1, we design an overall three-step workflow (Scheme 2) to identify Z-scheme heterostructures from 153 vdW heterostructures composed by 18 2D materials. To meet criterion 1, we apply

Anderson’s rule and predict that 112 over 153 heterostructures exhibit type-II band alignment. In the second step for meeting criterion 2, we use $\Delta V > 0.4$ eV to filter out 39 potential candidates with a low transfer barrier for the Z-scheme pathway. Lastly, by comparing $\Delta\chi_m > 0.05$ and determining the electron transfer direction (to satisfy criterion 3), we identify 27 Z-scheme heterostructures (Supporting Information, refer to Table S1). It is worth noting that three of them, CrS₂/MoSe₂, CrS₂/MoTe₂, and ZrS₂/WS₂, have already been reported as Z-scheme heterostructures in the literature,^{43,44} validating our descriptors, while 24 Z-scheme heterostructures have heterostructures with lattice mismatch below 5%. Ultimately, we recognize six exceptional Z-scheme heterostructures, MoS₂/TiS₂, TiSe₂/WSe₂, TiSe₂/MoSe₂, CrSe₂/TiS₂, TiS₂/WS₂, and TiS₂/MoSe₂. In the following, we will show the detailed method to find descriptors for discovering Z-scheme heterostructures and discuss the two descriptors ΔV and $\Delta\chi_m$ in detail.

We start from 18 MoS₂-like nonmagnetic H-phase TMD semiconductors because they have been synthesized experimentally.^{29,30} We systematically calculate their geometric structure, electronic structure, and magnetic properties using the DFT+HSE hybrid functional. Table 1 lists the 18 materials and their calculated properties, including lattice parameters, HSE band gap, gap type, conduction band minimum (CBM), and valence band maximum (VBM) positions relative to the vacuum level, as well as magnetic ordering. The h-TMD material is the H-phased MX₂ (such as 2H-MoS₂), in which an M-layer is covalently bonded to an X-layer, resulting in Bernal (ABA) stacking and belonging to the P₆m2 space group. The lattice parameters and HSE06 band gaps of these structures range between 3.05 and 4.88 Å and 0.89 and 2.28 eV, respectively. The VBM and CBM values span from -5.26 to -7.94 eV and -3.85 to -5.99 eV, respectively, making these materials suitable for heterostructure photocatalysts. Note that

Scheme 2. Overall Workflow for Identifying Z-Scheme Heterostructures in This Work^a



^aΔV represents the difference between E_{cc} and E_{cv} , where E_{cc} is the difference between the CB of OP and the CB of RP and E_{cv} represents the difference between the CB of OP and the VB of RP. $\Delta\chi_m$ represents the difference between $\chi_{(OP)}$ and $\chi_{(RP)}$. $\chi_{(OP)}$ and $\chi_{(RP)}$ represent Allen material electronegativity (χ_m) of OP and RP, respectively. χ_m is a novel descriptor proposed by us to predict the charge transfer direction in the heterostructure.

all 18 h-TMD materials and some of their heterostructures have already been synthesized experimentally using the universal chemical vapor deposition method.^{29,30}

Figure 1a exhibits the formation of 153 vdW 2D heterostructures, which result from pairing 18 H-phase TMDs. Previous research works have indicated that stacking configurations have a minimal influence on the electronic structure of h-TMD vdW heterostructures.^{45–47} For example, the band structure of a heterostructure is a simple superposition of 2D material layers due to the weak vdW interaction.^{47,48} In order to discover Z-scheme heterostructures from the 153 heterostructures, it is essential to first identify their parent structures: type-II heterostructures. Thus, we classify the 153 vdW heterostructures into type-I, type-II, and type-III (Figure 1b) based on the HSE band edge of each 2D material and Anderson's rule.⁴⁹ Anderson's rule serves as a distinctive physical model in the data-driven discovery of 2D functional heterostructures, which are connected by weak vdW interactions, preserving their intrinsic electronic structure and weak interfacial charge transfer.^{50–52} Figure 1b illustrates 19 type-I (straddling alignment), 112 type-II (staggered alignment), and 22 type-III (broken alignment) heterostructures from total 153 heterostructures. It is worth noting that type-I and type-III heterostructures are unsuitable for photocatalysis applications because of their charge transfer pathways, which

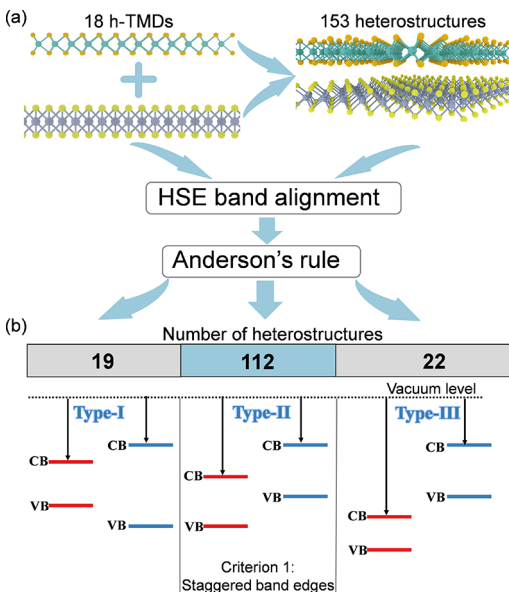


Figure 1. (a) Detailed diagram depicting the 153 vdW heterostructures formed by 18 individual monolayer TMDs. (b) Classification of heterostructures into three types based on Anderson's rule. Type-II heterostructures (112) are screened out in a pool for further identifying Z-scheme heterostructures.

cannot spatially separate photogenerated electrons and holes, thus not impeding their recombination. Therefore, our following study focuses exclusively on the 112 type-II band alignment heterostructures.

To accurately predict band alignment in heterostructures and identify appropriate Z-scheme candidates, we suggest the use of ΔV, as depicted in Figure 2a, rather than utilizing δ (or E_{CV}) as stated in Scheme 1. This is because carriers will follow the type-II pathway if E_{CC} is smaller than E_{CV} , even in cases where δ or E_{CV} is small. A larger value of ΔV indicates a closer conduction band (CB) of OP to the valence band (VB) of RP and a greater distance from the CB of RP. This suggests facilitated electron transfer from the CB of OP to the VB of RP while hindering electron transfer from the CB of RP to the CB of OP. Consequently, the heterostructure is of the Z-scheme type. The value of ΔV is critical in screening potential Z-scheme candidates. A high ΔV may exclude relevant candidates, while an excessively low value may include non-Z-scheme candidates. As shown in Table S2, gradually increasing ΔV ($\Delta\chi_m$) from 0 (0 eV) to 1.0 eV (0.10 eV) reduces the screened Z-scheme heterostructures from 43 to 5. Upon such analysis, our results confirm that setting ΔV above 0.6 eV may exclude many Z-scheme heterostructures, such as HfS₂/MoS₂ (ΔV = 0.497 eV) and CrS₂/MoSe₂.⁴³ Conversely, setting ΔV below 0.2 eV may include non-Z-scheme heterostructures, such as MoS₂/WTe₂ (ΔV = 0.08 eV). Therefore, we rationally select ΔV = 0.4 eV as the optimized value for screening Z-scheme heterostructures (Scheme 2).

Most importantly, to predict the charge transfer direction in the heterostructure for determining the Z-scheme type, we propose a novel descriptor: Allen material electronegativity (χ_m), derived from Allen element electronegativity (χ_e).^{53–55} Allen element electronegativity primarily relies on the average energy of the valence electrons in free atoms. The rationale for employing Allen electronegativity is the principle of energy transfer from high to low levels, including valence electron

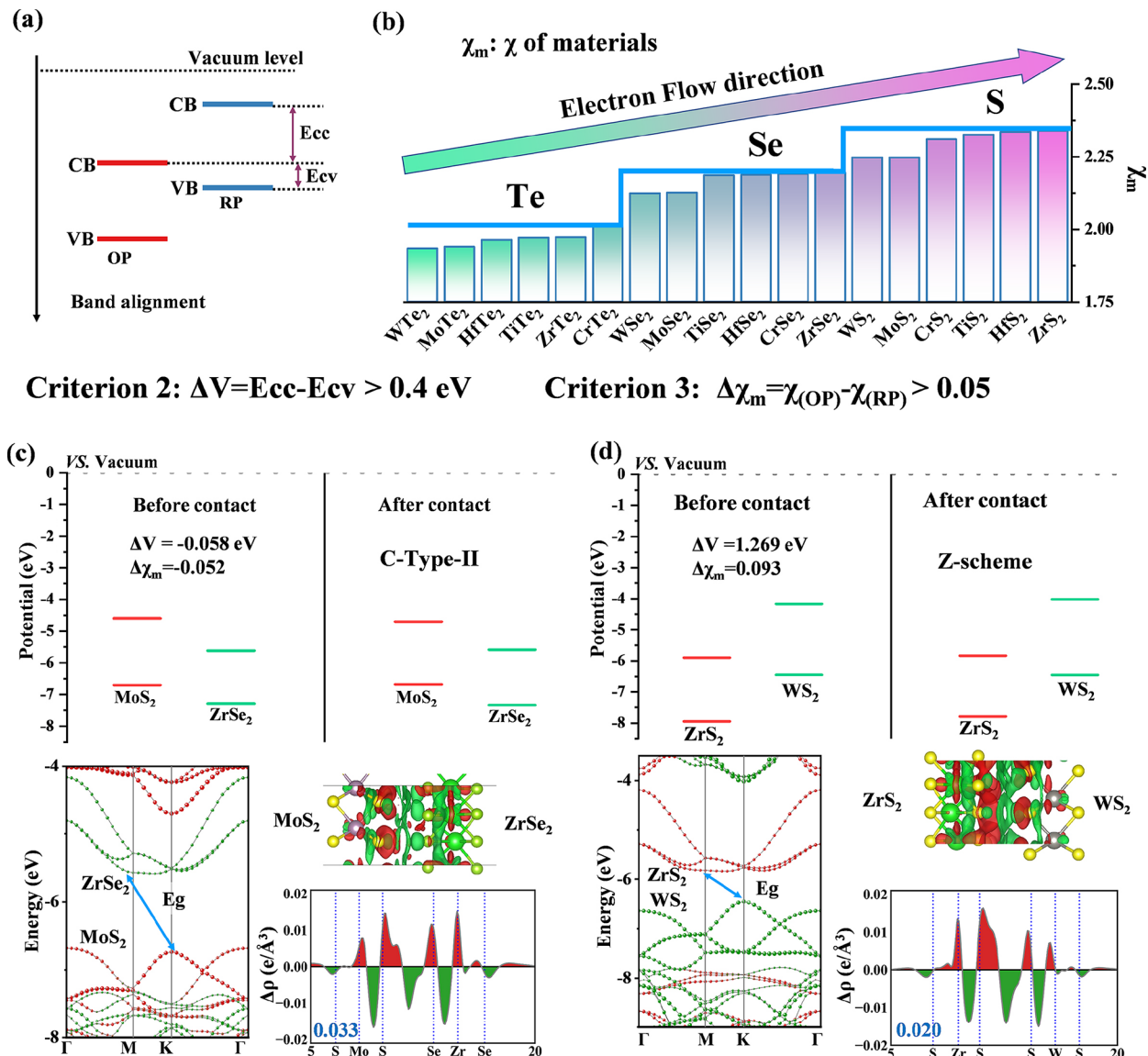


Figure 2. (a) Criteria of band alignment. (b) Allen material electronegativity of 18 h-TMD materials. Calculated electronic structures of (c) MoS₂/ZrSe₂ and (d) MoSe₂/TiSe₂, including HSE band structures, charge transfer difference, plane-integrated electron density difference along the vertical direction, and band alignment. The red and green regions represent electron accumulation and depletion, respectively. The isosurface value is $\pm 0.0001 \text{ e Å}^{-3}$. The number labeled in blue is the amount of the interlayer charge transfer calculated by the Bader charge analysis.

energy. The χ_m for the 18 MX₂-type h-TMD materials is calculated using the formula, as expressed,

$$\chi_m = \frac{(n_{sm}\epsilon_{sm} + n_{dm}\epsilon_{dm}) + 2(n_{sx}\epsilon_{sx} + n_{px}\epsilon_{px})}{(n_{sm} + n_{dm}) + 2(n_{sx} + n_{px})}$$

where $\epsilon_{sm,dm,sx,px}$ are the one-electron energy of s and d electrons in the M atom and s and p electrons in the X atom, respectively. $n_{sm,dm,sx,px}$ are the number of s and d electrons in the valence shell of M and s and p electrons in the valence shell of X, respectively. The one-electron energy can be determined directly from spectroscopic data, which are available for most elements. The number of s, p, and d electrons can be obtained through the Bader charge analysis (see in Table S3 for more details). Overall, we develop a novel method to estimate the material electronegativity.

The trend of χ_m is that higher χ_m corresponds to a greater tendency to attract electrons. Additionally, a larger difference in χ_m between the two materials comprising the hetero-

structure leads to more charge transfer and a large interfacial electric field. Figure 2b presents a summary of χ_m for 18 h-TMD materials, arranged in ascending order, and highlights the direction of electron flow in the resulting heterostructure upon contact. Note that the χ_m trend follows the order MT₂ < MS₂ < MS₂, (M = Ti, Zr, Hf, Cr, Mo, and W) due to the increased Allen element electronegativity from Te (2.158) to Se (2.424) and S (2.589), indicating that the anion has a more substantial impact on χ_m . Therefore, the charge transfer direction can be predicted simply based on the electronegativity of surface atoms when two materials with different surface atomic elements form a heterostructure. This prediction has been validated by numerous vdW heterostructure reports, including MoSe₂/SnS₂, MoSe₂/CrS₂, MoTe₂/SnS₂, MoTe₂/SnSe₂, MoTe₂/CrS₂, PtSe₂/WS₂, MoTe₂/ZrS₂, MoTe₂/NbSe₂, and MoS₂/In₂Se₃.^{43,44,56,57} However, for two materials with the same surface atom, such as MoTe₂ and WTe₂, the Allen element electronegativity is not

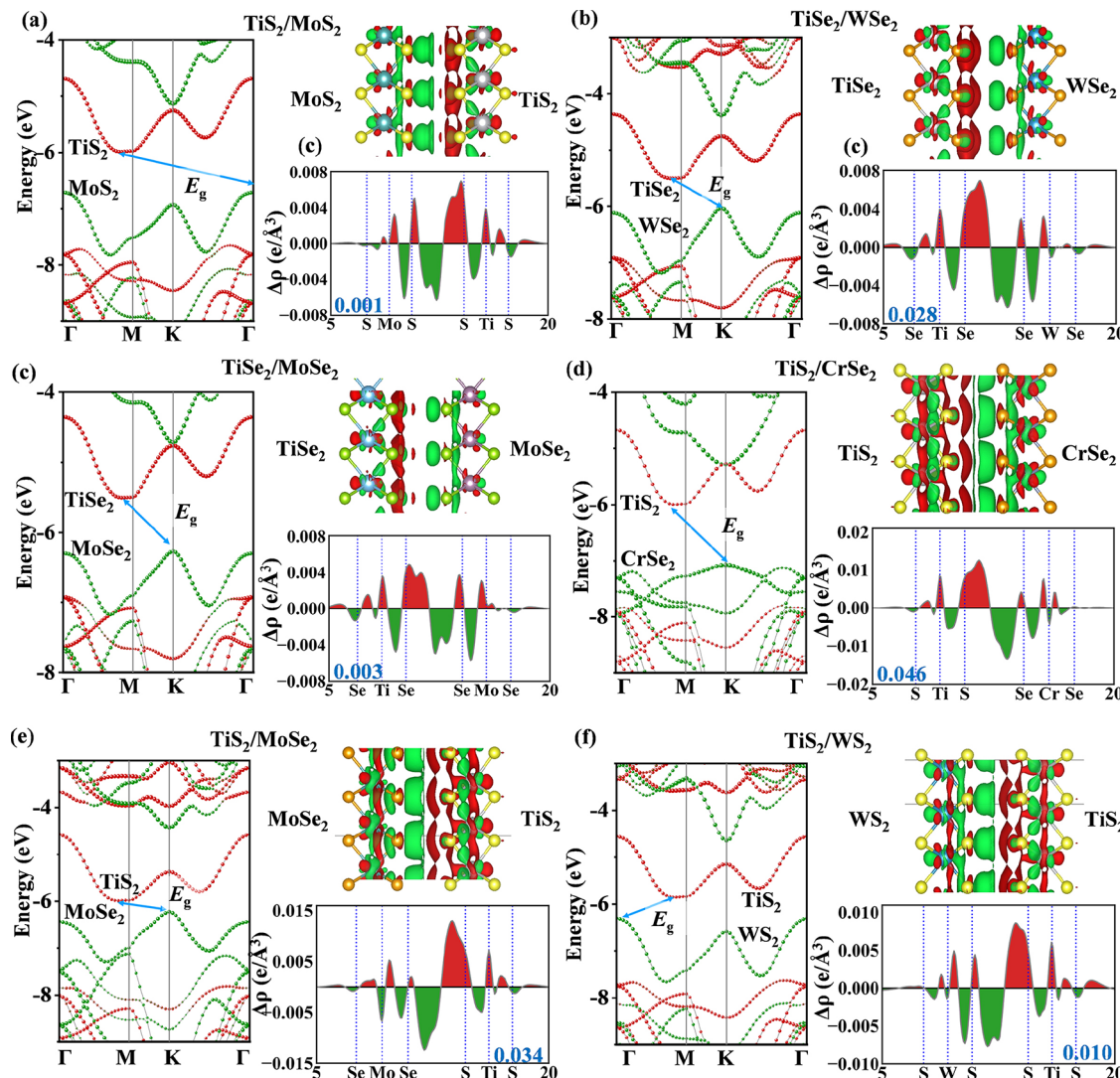


Figure 3. Calculated electronic structures of six identified candidates (a) TiS₂/MoS₂, (b) TiSe₂/WSe₂, (c) TiSe₂/MoSe₂, (d) TiS₂/CrSe₂, (e) TiS₂/MoSe₂, and (f) TiS₂/WS₂, including HSE band structures, charge transfer difference, and plane-integrated electron density difference along the out-of-plane direction. The red and green regions represent electron accumulation and depletion, respectively. The isosurface value is $\pm 0.0001 \text{ e \AA}^{-3}$. The amount of the interlayer charge transfer calculated by the Bader charge analysis is highlighted in blue.

applicable, and only the universal Allen “material” electronegativity can be used to predict the trend of the charge transfer and interface electric field between these two materials.

Considering the aforementioned understanding, we propose using the material electronegativity difference of two 2D materials, $\Delta\chi_m = \chi_{(\text{OP})} - \chi_{(\text{RP})}$, as a descriptor for predicting the charge transfer direction in the heterostructure (Figure 2b). A larger value of $\Delta\chi_m$ is expected to correspond to a more definite charge transfer direction from a material with lower χ_m to one with higher χ_m . However, if $\Delta\chi_m$ is too small, accurately determining the electron transfer direction may be difficult. Consequently, it is crucial to select an appropriate value for reliable charge transfer direction prediction. To validate this descriptor $\Delta\chi_m$, we systematically calculate and analyze HSE electronic structures of 20 heterostructures out of 112 type-II vdW heterostructures (see details in Table 2). It is worth noting that the HSE calculation of supercells for all 112 heterostructures is too computing expensive. The selection criteria for the 20 heterostructures are as follows: (1) including the well-reported materials, MoS₂ and TiS₂ (around 25 and 15% in the 112 type-II heterostructures), (2) excluding less

commonly utilized materials, such as TiTe₂, ZrTe₂, HfTe₂, and CrTe₂, and (3) a uniform distribution of the 20 calculated heterostructures to the 112 heterostructures. Because of the lattice mismatch, we perform various supercell expansion combinations for different pairings to maintain the lattice mismatch within a reasonable range (-4.97 to 5.28%). Table 2 shows the 20 supercells comprising $(1 \times 1 \times 1)(1 \times 1 \times 1)$, $(2 \times 2 \times 1)(\sqrt{3} \times \sqrt{3} \times 1)$, and $(3 \times 3 \times 1)(\sqrt{7} \times \sqrt{7} \times 1)$ configurations, containing 6, 21, and 48 atoms in these heterostructures, respectively. Furthermore, the lattice parameters and interlayer distances of these systems range from 3.27 to 9.48 Å and 3.27 to 3.80 Å, respectively. The binding energy (E_b) varies within a narrow range of -25.18 to -31.44 meV per atom, indicating that these heterostructures are representative vdW heterostructures.

We further conduct an in-depth study on the charge transfer and $\Delta\chi_m$ relationship in the 20 calculated heterostructures. As shown in Table 2, $\Delta\chi_m$ and ΔQ range from -0.001 to 0.314 and 0.001 to 0.115 e, respectively. It is worth noting that a larger χ_m indicates a higher probability of electron transfer to the material. Moreover, the band gaps of these heterostructures

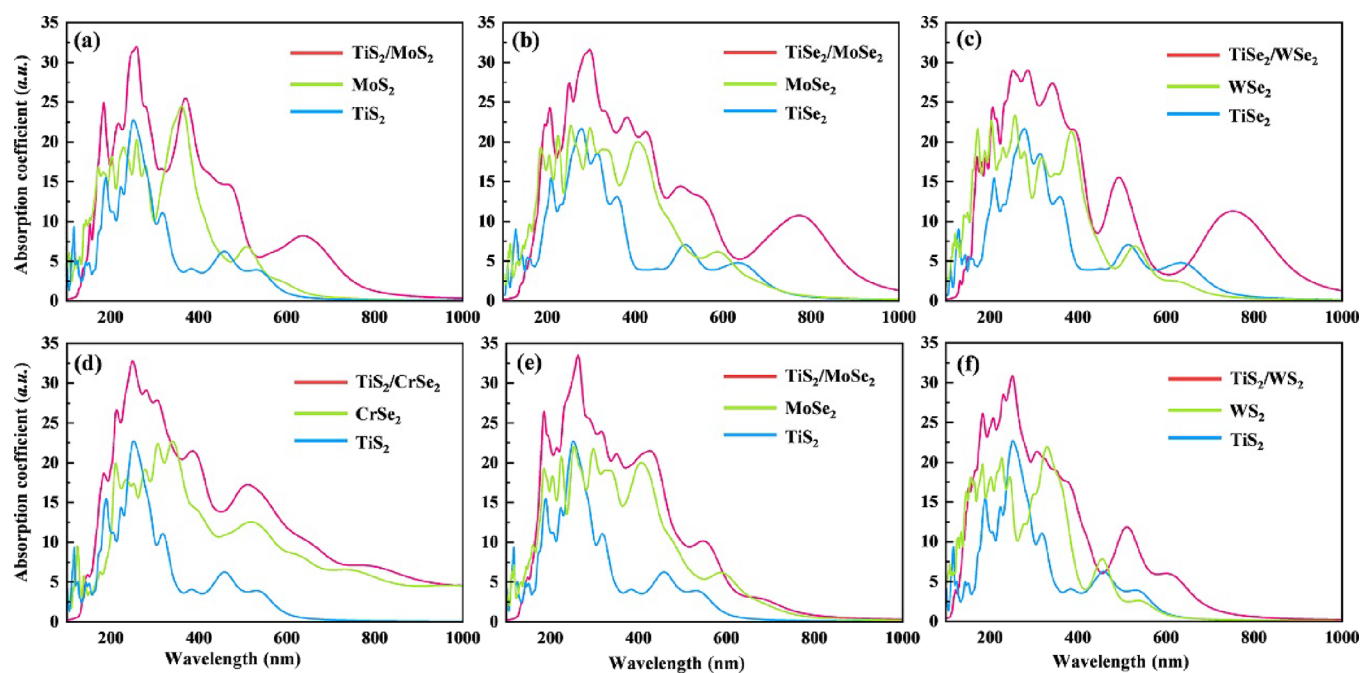


Figure 4. Calculated absorption coefficients of the six best Z-scheme heterostructure candidates (a) $\text{TiS}_2/\text{MoS}_2$, (b) $\text{TiSe}_2/\text{MoSe}_2$, (c) $\text{TiSe}_2/\text{WSe}_2$, (d) $\text{TiS}_2/\text{CrSe}_2$, (e) $\text{TiS}_2/\text{MoSe}_2$, and (f) TiS_2/WS_2 .

span from 0.23 to 1.79 eV, suggesting their potential as photocatalysts with suitable energy levels for producing photogenerated carriers. It is important to note that the χ_m of MoS_2 (2.247) is close to that of WS_2 (2.246), resulting in a $\Delta\chi_m$ of 0.001. On the one hand, this tiny $\Delta\chi_m$ makes it challenging to accurately predict the charge transfer direction between MoS_2 and WS_2 , consistent with our DFT calculations for this heterostructure (evidenced by a charge transfer of merely 0.001 e as determined by Bader analysis; see Table 2 and Figures S1–S12). On the other hand, a large $\Delta\chi_m$ (>0.1) may cause us to overlook some Z-scheme heterostructure candidates, such as the following confirmed Z-scheme heterostructures: $\text{TiSe}_2/\text{WSe}_2$ (0.063), $\text{TiS}_2/\text{MoS}_2$ (0.079), $\text{TiSe}_2/\text{MoSe}_2$ (0.06), ZrS_2/WS_2 (0.093), and $\text{HfS}_2/\text{MoS}_2$ (0.088). Overall, we establish that $\Delta\chi_m > 0.05$ is the more appropriate criterion for predicting the charge transfer direction (Scheme 2).

Figure 2c,d shows the DFT electronic structures of two representative heterostructures— $\text{MoS}_2/\text{ZrSe}_2$ as a C-type-II heterostructure and ZrS_2/WS_2 as a Z-scheme heterostructure—to validate the proposed ΔV and $\Delta\chi_m$ descriptors. Figure 2c demonstrates that $\text{MoS}_2/\text{ZrSe}_2$ is a typical C-type-II heterostructure due to its band alignment and charge transfer pathway. The VBM and CBM primarily consist of MoS_2 and ZrSe_2 , respectively, leading to a staggered band gap. Charge transfer, plane-integrated electron density difference, and Bader charge analysis all reveal that MoS_2 , acting as an acceptor, gains electrons and has a VBM positioned higher than that of ZrSe_2 (donor). In contrast, for ZrS_2/WS_2 (Figure 2d), the VBM and CBM are composed of WS_2 and ZrS_2 , respectively. This heterostructure displays a staggered band gap, like $\text{MoS}_2/\text{ZrSe}_2$. However, electrons accumulate on the ZrS_2 side (from the WS_2 donor) with a lower CBM and VBM position than WS_2 , resulting in charge transfer in the opposite direction of $\text{MoS}_2/\text{ZrSe}_2$. This observation indicates that ZrS_2/WS_2 is a typically Z-scheme heterostructure.

To validate the accuracy of the screening results, we perform high-fidelity DFT calculations on these six heterostructure candidates (Scheme 2), including HSE band structures, band alignment, and charge transfer as shown in Figure 3a–f. In the case of $\text{TiS}_2/\text{MoS}_2$ (Figure 3a), the VBM and CBM consist of MoS_2 and TiS_2 , respectively. The band structure of this heterostructure displays a staggered band gap. The band alignment and formation of a built-in electric field from MoS_2 to TiS_2 indicate that the $\text{TiS}_2/\text{MoS}_2$ heterostructure has typical Z-scheme behavior. The other five heterostructures also display similar band alignments and built-in electric fields, suggesting that they also are Z-scheme heterostructures, validating the accuracy of descriptors.

In a short summary, the aforementioned findings indicate that using ΔV and $\Delta\chi_m$ to forecast band alignment and charge transfer between h-TMD 2D materials (or other 2D materials because of the universality of Allen material negativity) is highly accurate and verifiable, making it a valuable tool for quick identifying suitable combinations before contact that could potentially serve as photocatalysts. The efficacy of the proposed time-saving descriptor approach is validated by both previous reports^{43,44} and our DFT calculations.

Optical absorption plays a crucial role in the initial stage of photocatalysis, as it offers insights into the properties of photocatalysts. Thus, we also investigate the optical absorption of the six best Z-scheme heterostructure candidates identified by descriptors. Figure 4 shows the absorption spectra of the six Z-scheme photocatalysts, and the optical absorption properties of these heterostructures have been thoroughly investigated. The optical absorption of $\text{MoS}_2/\text{TiS}_2$, $\text{TiSe}_2/\text{MoSe}_2$, and $\text{TiSe}_2/\text{WSe}_2$ heterostructures is enhanced in the visible-light range (300 to 600 nm) due to the small direct band gaps of MoS_2 (2.10 eV), MoSe_2 (1.83 eV), and WSe_2 (1.96 eV) monolayers. As indirect semiconductors, TiS_2 and TiSe_2 monolayers contribute minimally to absorption due to their weak absorption at the absorption edge. Interlayer excitation, or the transfer of electrons from the VB of one material to the

CB of the other, may also contribute to the absorption spectra in the infrared region, as observed in MoS₂/TiS₂, TiSe₂/MoSe₂, and TiSe₂/WSe₂ heterostructures (peaks at 641, 772, and 751 nm, respectively). However, it is worth noting that such a type of interlayer excitation is not useful for Z-scheme photocatalysts.

In contrast, the CrSe₂ monolayer exhibits direct semiconductor behavior with a small band gap of 1.04 eV, resulting in near-infrared light absorption (~700–1000 nm) in the CrSe₂/TiS₂ heterostructure. TiS₂/MoSe₂ and TiS₂/WS₂ heterostructures exhibit strong optical absorption in the visible- and ultraviolet-light range (~200 to 700 nm), with the primary absorption dominated by MoSe₂ and WS₂ monolayers. In this context, band positions with edges are considered to evaluate the feasibility of employing these photocatalysts for water catalytic applications (Figure S13). The results indicate that all six heterostructures displayed high potential for the oxygen evolution reaction. Among them, TiSe₂/WSe₂ and TiS₂/MoSe₂ demonstrate the capability to concurrently perform the hydrogen evolution reaction. Overall, the optical absorption properties of Z-scheme heterostructures are enhanced in the visible-light range due to the small direct band gaps of the monolayers forming the heterostructure. The CrSe₂/TiS₂ heterostructure exhibits near-infrared light absorption owing to the direct semiconductor behavior of the CrSe₂ monolayer. Note that further calculations on catalytic properties, such as the carrier mobility, exciton binding energy, and Gibbs free energy, are beyond the scope of this work, which focuses on developing descriptors to accelerate the discovery of Z-scheme vdW heterostructures. Nonetheless, we hope that our research will stimulate increased theoretical and experimental investigations into various photocatalytic applications involving Z-scheme vdW heterostructures.

CONCLUSIONS AND OUTLOOK

In summary, through a data-driven discovery approach, we develop a descriptor method for identifying Z-scheme vdW heterostructures before contact, bypassing the need of expensive high-fidelity calculations on heterostructure supercells. Using electronic structures of dozens of experimentally synthesized monolayer 2D materials and heterostructures, we propose the Allen “material” electronegativity difference $\Delta\chi_m$ as an efficient and effective descriptor for identifying Z-scheme heterostructures. Such a data-driven descriptor method allows us to identify 24 Z-scheme candidates, which have never been reported before. We finally screen six exceptional Z-scheme heterostructures—MoS₂/TiS₂, TiSe₂/WSe₂, TiSe₂/MoSe₂, CrSe₂/TiS₂, TiS₂/WS₂, and TiS₂/MoSe₂—all confirmed by DFT+HSE calculations. Among them, the CrSe₂/TiS₂ heterostructure demonstrates an outstanding photocatalytic activity due to its absorption of near-infrared light. Our findings not only contribute to the accelerated discovery of highly efficient heterostructure photocatalysts but also provide a universal descriptor for exploring charge transfer in 2D material interfaces, providing guidelines for nanodevice design.

In heterostructures composed of nonlayered materials and no interfacial chemical bonding, such as oxide/nitride Z-scheme heterojunctions, the direction of charge transfer can still be discerned through a variant descriptor of Allen material electronegativity of the materials’ surface atoms, termed “Allen surface electronegativity”. This is defined by the average energy of the valence electrons of all surface atoms of the materials. It is encouraged that more computational and experimental

studies adapt Allen material/surface electronegativity to further investigate charge transfer and internal electric fields across a wider range of material interfaces, including but not limited to layered van der Waals interfaces.

ASSOCIATED CONTENT

Supporting Information

The Supporting Information is available free of charge at <https://pubs.acs.org/doi/10.1021/acscatal.3c02315>.

Detailed calculation methods, Allen material electronegativity of single materials, predicted 27 Z-scheme heterostructures, and electronic structures of heterostructures’ band alignment of the best candidates ([PDF](#))

AUTHOR INFORMATION

Corresponding Authors

Miao Zhou – Key Laboratory of Optoelectronic Technology and System of Ministry of Education, College of Optoelectronic Engineering, Chongqing University, Chongqing 400044, P. R. China; Email: mzhou@cqu.edu.cn

Lei Shen – Department of Mechanical Engineering, National University of Singapore, 117575, Singapore; orcid.org/0000-0001-6198-5753; Email: shenlei@nus.edu.sg

Authors

Xiaoging Liu – Key Laboratory of Optoelectronic Technology and System of Ministry of Education, College of Optoelectronic Engineering, Chongqing University, Chongqing 400044, P. R. China; Department of Mechanical Engineering, National University of Singapore, 117575, Singapore

Yi-Ming Zhao – Department of Mechanical Engineering, National University of Singapore, 117575, Singapore; orcid.org/0000-0002-3921-1900

Xiuying Zhang – Department of Physics, National University of Singapore, 117542, Singapore

Lin Wang – Key Laboratory of Optoelectronic Technology and System of Ministry of Education, College of Optoelectronic Engineering, Chongqing University, Chongqing 400044, P. R. China

Jiadong Shen – Department of Mechanical Engineering, National University of Singapore, 117575, Singapore; orcid.org/0000-0003-4173-2016

Complete contact information is available at:

<https://pubs.acs.org/doi/10.1021/acscatal.3c02315>

Notes

The authors declare no competing financial interest.

ACKNOWLEDGMENTS

The authors thank Dr. Jun Zhou, Dr. Wang Xian, and Dr. Wang Peng for their helpful discussion. This work was supported by the Scientific and Technological Research Program of Chongqing Municipal Education Commission (Grant No. KJQN202000629) and the Natural Science Foundation of Chongqing (Grant No. cstc2020jcyj-msxmX0692). X.L. acknowledges financial support from the China Scholarship Council (no. 202106050115). The authors also acknowledge the Centre for Advanced 2D Materials (C2DHPC), High-Performance Computing of the National University of Singapore (HPC@NUS IT), and the National Supercomputing Centre Singapore (NSCC) for providing computing resources.

■ REFERENCES

- (1) Smalley, R. E. Future Global Energy Prosperity: The Terawatt Challenge. *MRS Bull.* **2005**, *30*, 412–417.
- (2) Dresselhaus, M. S.; Thomas, I. L. Alternative Energy Technologies. *Nature* **2001**, *414*, 332–337.
- (3) Zhao, Y.; Zhang, S.; Shi, R.; Waterhouse, G. I. N.; Tang, J.; Zhang, T. Two-Dimensional Photocatalyst Design: A Critical Review of Recent Experimental and Computational Advances. *Mater. Today* **2020**, *34*, 78–91.
- (4) Shi, L.; Guo, P.; Zheng, J.; Zhao, P.; Jiang, Z.; Shen, L. C60 Surface-Supported Tm@Si16 (TM = Ti, Zr, Hf) Superatoms as Self-Assembled Photocatalysts. *Appl. Surf. Sci.* **2023**, *616*, No. 156465.
- (5) Xu, Q.; Zhang, L.; Yu, J.; Wageh, S.; Al-Ghamdi, A. A.; Jaroniec, M. Direct Z-Scheme Photocatalysts: Principles, Synthesis, and Applications. *Mater. Today* **2018**, *21*, 1042–1063.
- (6) Low, J.; Yu, J.; Jaroniec, M.; Wageh, S.; Al-Ghamdi, A. A. Heterojunction Photocatalysts. *Adv. Mater.* **2017**, *29*, 1601694.
- (7) Su, T.; Shao, Q.; Qin, Z.; Guo, Z.; Wu, Z. Role of Interfaces in Two-Dimensional Photocatalyst for Water Splitting. *ACS Catal.* **2018**, *8*, 2253–2276.
- (8) Fu, C.-F.; Wu, X.; Yang, J. Material Design for Photocatalytic Water Splitting from a Theoretical Perspective. *Adv. Mater.* **2018**, *30*, 1802106.
- (9) Zhou, P.; Yu, J.; Jaroniec, M. All-Solid-State Z-Scheme Photocatalytic Systems. *Adv. Mater.* **2014**, *26*, 4920–4935.
- (10) Iwase, A.; Yoshino, S.; Takayama, T.; Ng, Y. H.; Amal, R.; Kudo, A. Water Splitting and CO₂ Reduction under Visible Light Irradiation Using Z-Scheme Systems Consisting of Metal Sulfides, CoOx-Loaded BiVO₄, and a Reduced Graphene Oxide Electron Mediator. *J. Am. Chem. Soc.* **2016**, *138*, 10260–10264.
- (11) Wang, L.; Zheng, X.; Chen, L.; Xiong, Y.; Xu, H. Van Der Waals Heterostructures Comprised of Ultrathin Polymer Nanosheets for Efficient Z-Scheme Overall Water Splitting. *Angew. Chem., Int. Ed.* **2018**, *130*, 3512–3516.
- (12) Huang, Z.-F.; Song, J.; Wang, X.; Pan, L.; Li, K.; Zhang, X.; Wang, L.; Zou, J.-J. Switching Charge Transfer of C₃N₄/W₁₈O₄₉ from Type-II to Z-Scheme by Interfacial Band Bending for Highly Efficient Photocatalytic Hydrogen Evolution. *Nano Energy* **2017**, *40*, 308–316.
- (13) Di, T.; Xu, Q.; Ho, W.; Tang, H.; Xiang, Q.; Yu, J. Review on Metal Sulphide-Based Z-Scheme Photocatalysts. *ChemCatChem* **2019**, *11*, 1394–1411.
- (14) Qiao, M.; Liu, J.; Wang, Y.; Li, Y.; Chen, Z. PdSeO₃ Monolayer: Promising Inorganic 2D Photocatalyst for Direct Overall Water Splitting without Using Sacrificial Reagents and Cocatalysts. *J. Am. Chem. Soc.* **2018**, *140*, 12256–12262.
- (15) Gao, X.; Shen, Y.; Liu, J.; Lv, L.; Zhou, M.; Zhou, Z.; Feng, Y. P.; Shen, L. Boosting photon absorption, exciton dissociation, and photocatalytic hydrogen and oxygen evolution reactions by build-in electric fields in Janus platinum dichalcogenides. *J. Mater. Chem. C* **2021**, *9*, 15026–15033.
- (16) Gao, X.; Shen, Y.; Liu, J.; Lv, L.; Zhou, M.; Zhou, Z.; Feng, Y. P.; Shen, L. Developing Dipole-scheme Heterojunction Photocatalysts. *Appl. Surf. Sci.* **2022**, *599*, No. 153942.
- (17) Hastrup, S.; Strange, M.; Pandey, M.; Deilmann, T.; Schmidt, P. S.; Hinsche, N. F.; Gjerding, M. N.; Torelli, D.; Larsen, P. M.; Riis-Jensen, A. C.; et al. The Computational 2D Materials Database: High-Throughput Modeling and Discovery of Atomically Thin Crystals. *2D Mater.* **2018**, *5*, No. 042002.
- (18) Shen, L.; Zhou, J.; Yang, T.; Yang, M.; Feng, Y. P. High-Throughput Computational Discovery and Intelligent Design of Two-Dimensional Functional Materials for Various Applications. *Acc. Mater. Res.* **2022**, *3*, 572.
- (19) Zhou, J.; Shen, L.; Costa, M. D.; Persson, K. A.; Ong, S. P.; Huck, P.; Lu, Y.; Ma, X.; Chen, Y.; Tang, H.; et al. 2Dmatpedia, an Open Computational Database of Two-Dimensional Materials from Top-Down and Bottom-up Approaches. *Sci. Data* **2019**, *6*, 86.
- (20) Choudhary, K.; Garrity, K. F.; Reid, A. C. E.; DeCost, B.; Biacchi, A. J.; Hight Walker, A. R.; Trautt, Z.; Hattrick-Simpers, J.; Kusne, A. G.; Centrone, A.; et al. The Joint Automated Repository for Various Integrated Simulations (Jarvis) for Data-Driven Materials Design. *npj Comput. Mater.* **2020**, *6*, 173.
- (21) Butler, K. T.; Davies, D. W.; Cartwright, H.; Isayev, O.; Walsh, A. Machine Learning for Molecular and Materials Science. *Nature* **2018**, *559*, 547–555.
- (22) Gubernatis, J. E.; Lookman, T. Machine Learning in Materials Design and Discovery: Examples from the Present and Suggestions for the Future. *Phys. Rev. Mater.* **2018**, *2*, No. 120301.
- (23) Jain, A.; Ong, S. P.; Hautier, G.; Chen, W.; Richards, W. D.; Dacek, S.; Cholia, S.; Gunter, D.; Skinner, D.; Ceder, G.; et al. Commentary: The Materials Project: A Materials Genome Approach to Accelerating Materials Innovation. *APL Mater.* **2013**, *1*, No. 011002.
- (24) Curtarolo, S.; Hart, G. L. W.; Nardelli, M. B.; Mingo, N.; Sanvito, S.; Levy, O. The High-Throughput Highway to Computational Materials Design. *Nat. Mater.* **2013**, *12*, 191–201.
- (25) Giovannetti, G.; Khomyakov, P. A.; Brocks, G.; Karpan, V. M.; van den Brink, J.; Kelly, P. J. Doping Graphene with Metal Contacts. *Phys. Rev. Lett.* **2008**, *101*, No. 026803.
- (26) Sun, H.; Shang, Y.; Yang, Y.; Guo, M. Realization of N-type Semiconducting of Phosphorene Through Surface Metal Doping and Work Function Study. *J. Nanomater.* **2018**, *2018*, 1–9.
- (27) Ghosh, S.; Mammen, N.; Narasimhan, S. Descriptor for the Efficacy of Aliovalent Doping of Oxides and Its Application for the Charging of Supported Au Clusters. *J. Phys. Chem. C* **2019**, *123*, 19794–19805.
- (28) Sharma, D.; Gautam, G.; Narasimhan, S. A Simple Descriptor for Binding and Charge Transfer at Blue Phosphorene-Metal Interfaces. *Appl. Surf. Sci.* **2019**, *492*, 16–22.
- (29) Zhou, J.; Lin, J.; Huang, X.; Zhou, Y.; Chen, Y.; Xia, J.; Wang, H.; Xie, Y.; Yu, H.; Lei, J.; et al. A Library of Atomically Thin Metal Chalcogenides. *Nature* **2018**, *556*, 355–359.
- (30) Habib, M. R.; Wang, S.; Wang, W.; Xiao, H.; Obaidulla, S. M.; Gayen, A.; Khan, Y.; Chen, H.; Xu, M. Electronic Properties of Polymorphic Two-Dimensional Layered Chromium Disulphide. *Nanoscale* **2019**, *11*, 20123–20132.
- (31) Kresse, G.; Furthmüller, J. Efficient Iterative Schemes for Ab Initio Total-Energy Calculations Using a Plane-Wave Basis Set. *Phys. Rev. B* **1996**, *54*, 11169–11186.
- (32) Blöchl, P. E. Projector Augmented-Wave Method. *Phys. Rev. B* **1994**, *50*, 17953–17979.
- (33) Payne, M. C.; Teter, M. P.; Allan, D. C.; Arias, T. A.; Joannopoulos, J. D. Iterative Minimization Techniques for Ab initio Total-Energy Calculations - Molecular-Dynamics and Conjugate Gradients. *Rev. Mod. Phys.* **1992**, *64*, 1045–1097.
- (34) Paier, J.; Marsman, M.; Hummer, K.; Kresse, G.; Gerber, I. C.; Ángyán, J. G. Screened Hybrid Density Functionals Applied to Solids. *J. Chem. Phys.* **2006**, *124*, 154709–154700.
- (35) Perdew, J. P.; Ruzsinszky, A.; Csonka, G. I.; Vydrov, O. A.; Scuseria, G. E.; Constantin, L. A.; Zhou, X.; Burke, K. Restoring the Density-Gradient Expansion for Exchange in Solids and Surfaces. *Phys. Rev. Lett.* **2008**, *100*, No. 136406.
- (36) Klimeš, J.; Bowler, D. R.; Michaelides, A. Chemical Accuracy for the Van Der Waals Density Functional. *J. Phys.: Condens. Matter* **2010**, *22*, No. 022201.
- (37) Momma, K.; Izumi, F. Vesta: A Three-Dimensional Visualization System for Electronic and Structural Analysis. *J. Appl. Crystallogr.* **2008**, *41*, 653–658.
- (38) Wang, V.; Xu, N.; Liu, J.-C.; Tang, G.; Geng, W.-T. Vaspkit: A User-Friendly Interface Facilitating High-Throughput Computing and Analysis Using Vasp Code. *Comput. Phys. Commun.* **2021**, *267*, No. 108033.
- (39) Tang, W.; Sanville, E.; Henkelman, G. A Grid-Based Bader Analysis Algorithm without Lattice Bias. *J. Phys.: Condens. Matter* **2009**, *21*, No. 084204.
- (40) Sanville, E.; Kenny, S. D.; Smith, R.; Henkelman, G. Improved Grid-Based Algorithm for Bader Charge Allocation. *J. Comput. Chem.* **2007**, *28*, 899–908.

- (41) Henkelman, G.; Arnaldsson, A.; Jónsson, H. A Fast and Robust Algorithm for Bader Decomposition of Charge Density. *Comput. Mater. Sci.* **2006**, *36*, 354–360.
- (42) Gao, X.; Shen, Y.; Liu, J.; Lv, L.; Zhou, M.; Zhou, Z.; Feng, Y. P.; Shen, L. Boost the Large Driving Photovoltages for Overall Water Splitting in Direct Z-scheme Heterojunctions by Interfacial Polarization. *Catal. Sci. Technol.* **2022**, *12*, 3614–3621.
- (43) Fu, C.-F.; Zhang, R.; Luo, Q.; Li, X.; Yang, J. Construction of Direct Z-scheme Photocatalysts for Overall Water Splitting Using Two-Dimensional Van Der Waals Heterojunctions of Metal Dichalcogenides. *J. Comput. Chem.* **2019**, *40*, 980–987.
- (44) Zhang, C.; Gong, C.; Nie, Y.; Min, K.-A.; Liang, C.; Oh, Y. J.; Zhang, H.; Wang, W.; Hong, S.; Colombo, L.; et al. Systematic Study of Electronic Structure and Band Alignment of Monolayer Transition Metal Dichalcogenides in Van Der Waals Heterostructures. *2D Mater.* **2017**, *4*, No. 015026.
- (45) Conte, F.; Ninno, D.; Cantele, G. Electronic Properties and Interlayer Coupling of Twisted MoS₂/NbSe₂ Heterobilayers. *Phys. Rev. B* **2019**, *99*, No. 155429.
- (46) Chen, Y.; Sun, M. Two-Dimensional WS₂/MoS₂ Heterostructures: Properties and Applications. *Nanoscale* **2021**, *13*, 5594–5619.
- (47) Ganesan, V. D. S.; Linghu, J.; Zhang, C.; Feng, Y. P.; Shen, L. Heterostructures of Phosphorene and Transition Metal Dichalcogenides for Excitonic Solar Cells: A First-Principles Study. *Appl. Phys. Lett.* **2016**, *108*, 122105.
- (48) Linghu, J.; Yang, T.; Luo, Y.; Yang, M.; Zhou, J.; Shen, L.; Feng, Y. P. High-Throughput Computational Screening of Vertical 2D van der Waals Heterostructures for High-efficiency Excitonic Solar Cells. *ACS Appl. Mater. Interfaces* **2018**, *10*, 32142–32150.
- (49) Schlaf, R.; Lang, O.; Pettenkofer, C.; Jaegermann, W. Band Lineup of Layered Semiconductor Heterointerfaces Prepared by Van Der Waals Epitaxy: Charge Transfer Correction Term for the Electron Affinity Rule. *J. Appl. Phys.* **1999**, *85*, 2732–2753.
- (50) Dong, R.; Jacob, A.; Bourdais, S.; Sanvito, S. High-Throughput Bandstructure Simulations of Van Der Waals Hetero-Bilayers Formed by 1T and 2H Monolayers. *npj 2D Mater. Appl.* **2021**, *5*, 26.
- (51) Ge, L.; Yuan, H.; Min, Y.; Li, L.; Chen, S.; Xu, L.; Goddard, W. A. Predicted Optimal Bifunctional Electrocatalysts for the Hydrogen Evolution Reaction and the Oxygen Evolution Reaction Using Chalcogenide Heterostructures Based on Machine Learning Analysis of in Silico Quantum Mechanics Based High Throughput Screening. *J. Phys. Chem. Lett.* **2020**, *11*, 869–876.
- (52) Thygesen, K. S. Calculating Excitons, Plasmons, and Quasiparticles in 2D Materials and Van Der Waals Heterostructures. *2D Mater.* **2017**, *4*, No. 022004.
- (53) Allen, L. C. Electronegativity Is the Average One-Electron Energy of the Valence-Shell Electrons in Ground-State Free Atoms. *J. Am. Chem. Soc.* **1989**, *111*, 9003–9014.
- (54) Mann, J. B.; Meek, T. L.; Allen, L. C. Configuration Energies of the Main Group Elements. *J. Am. Chem. Soc.* **2000**, *122*, 2780–2783.
- (55) Mann, J. B.; Meek, T. L.; Knight, E. T.; Capitani, J. F.; Allen, L. C. Configuration Energies of the D-Block Elements. *J. Am. Chem. Soc.* **2000**, *122*, 5132–5137.
- (56) Qiao, H.; Zhang, Y.; Yan, Z.-H.; Duan, L.; Fan, J.-B.; Ni, L. The Type-II PtSe₂/WS₂ Van Der Waals Heterostructure: A High Efficiency Water-Splitting Photocatalyst. *Surf. Sci.* **2022**, *723*, No. 122103.
- (57) Shao, G.; Yang, M.; Xiang, H.; Luo, S.; Xue, X.-X.; Li, H.; Zhang, X.; Liu, S.; Zhou, Z. Edge Reconstruction of Layer-Dependent β -In₂Se₃/MoS₂ Vertical Heterostructures for Accelerated Hydrogen Evolution. *Nano Res.* **2023**, *16*, 1670–1678.